SCIENTIFIC REP**O**RTS

OPEN

Low content Pt nanoparticles anchored on N-doped reduced graphene oxide with high and stable electrocatalytic activity for oxygen reduction reaction

Zeyu Li[1,2], Qiuming Gao[1], Hang Zhang[1], Weiqian Tian[1], Yanli Tan[1], Weiwei Qian[1] & Zhengping Liu[2]

A novel kind of Pt/N-rGO hybrid possessing of low content 5.31 wt.% Pt anchored on the surface of nitrogen doped reduced graphene oxide (N-rGO) evenly was prepared. The Pt has uniformed 2.8 nm diameter and exposed (111) crystal planes; meanwhile, the N works as the bridge between Pt and rGO with the Pt-N and N-C chemical bonds in Pt/N-rGO. The Pt/N-rGO material has a very high electrocatalytic activity in oxygen reduction reaction with the mass catalytic activity more than 1.5 times of the commercial Pt/C due to the synergistic catalytic effect of both N-doped carbon matrix and Pt nanoparticles. Moreover, the Pt/N-rGO exhibits an excellent stability with hardly loss (only 0.4%) after accelerated durability tests of 5000 cycles based on the stable Pt-N-C chemical bonds in Pt/N-rGO, which can prevent the detachment, dissolution, migration and aggregation of Pt nanoparticles on the matrix during the long-term cycling.

Platinum particles have shown a good electrocatalytic activity in oxygen reduction reaction (ORR) which is the key reaction over the cathode in fuel cells and/or metal-air batteries, *e.g.*, Li-O$_2$ battery, due to the incompletely filled *d*-orbital leading to the moderate adsoption[1,2]. The matrixes such as carbon-based materials with large surface areas and high electric conductivities are very important for the Pt catalysts to be loaded on ref. 3. Graphene with a two-dimensional (2D) nanosheet structure demonstrates large surface area, high electric conductivity and high mechanical strength, becoming a good choice as the supporting material for the precious metal catalysts[4,5]. In order to further enhance the activity and durability of the catalysts, heteroatom-doped graphene could be used as the supporting material [6,7]. Nitrogen was chosen as the important dopant element due to the similar size to carbon and one electron more than carbon in the external shell[8]. Beyond the matrix effect, among the different types of doped N, pyridinic and pyrrolic N as well as the carbon atoms next to them have contributed greatly to the ORR catalytic activity[9–14]. As to the Pt particles, both the particle size[15–18] and the crystal faces[19,20] may greatly affect the catalytic activity.

However, there is no report on the ORR electrocatalytic catalyst with the aforementioned comprehensive ideal Pt particle size and the crystal faces as well as suitable matrix. Herein, we design the synthesis of Pt/N-rGO nanohybrid catalyst via a facile solvothermal method. The Pt/N-rGO nanomaterial possesses monodispersed Pt nanoparticles with the diammeter of 2.8 nm and exposed (111) facts on the N-doped reduced graphene oxide (N-rGO) nanosheets, which exhibited high ORR electrocatalytic activity and excellent stability after 5000 cycles.

[1]Key Laboratory of Bio-inspired Smart Interfacial Science and Technology of Ministry of Education, Beijing Key Laboratory of Bio-inspired Energy Materials and Devices, School of Chemistry and Environment, Beihang University, Beijing 100191, P.R. China. [2]Institute of Polymer Chemistry and Physics of College of Chemistry, BNU Lab of Environmentally Friendly and Functional Polymer Materials, Beijing Normal University, Beijing 100875, P.R. China. Correspondence and requests for materials should be addressed to Q.G. (email: qmgao@buaa.edu.cn) or Z.L. (email: lzp@bnu.edu.cn).
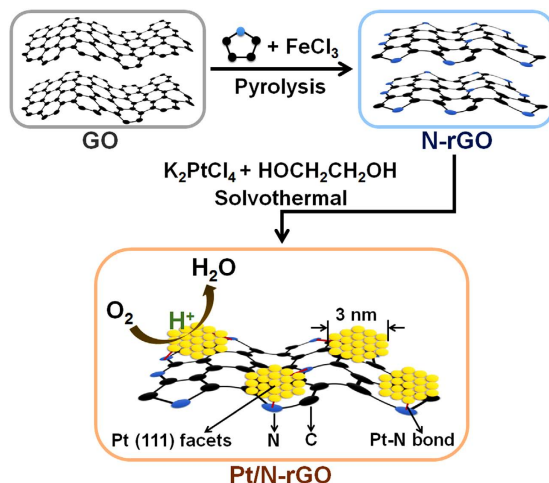
Figure 1. The synthesis and configuration of Pt/N-rGO performed as the catalyst of ORR. The Pt particles with uniformed 2.8 nm diameter and exposed (111) crystal planes anchored on the surface of N-rGO evenly. And the N works as the bridge between Pt and rGO with the Pt-N and N-C chemical bonds in Pt/N-rGO.
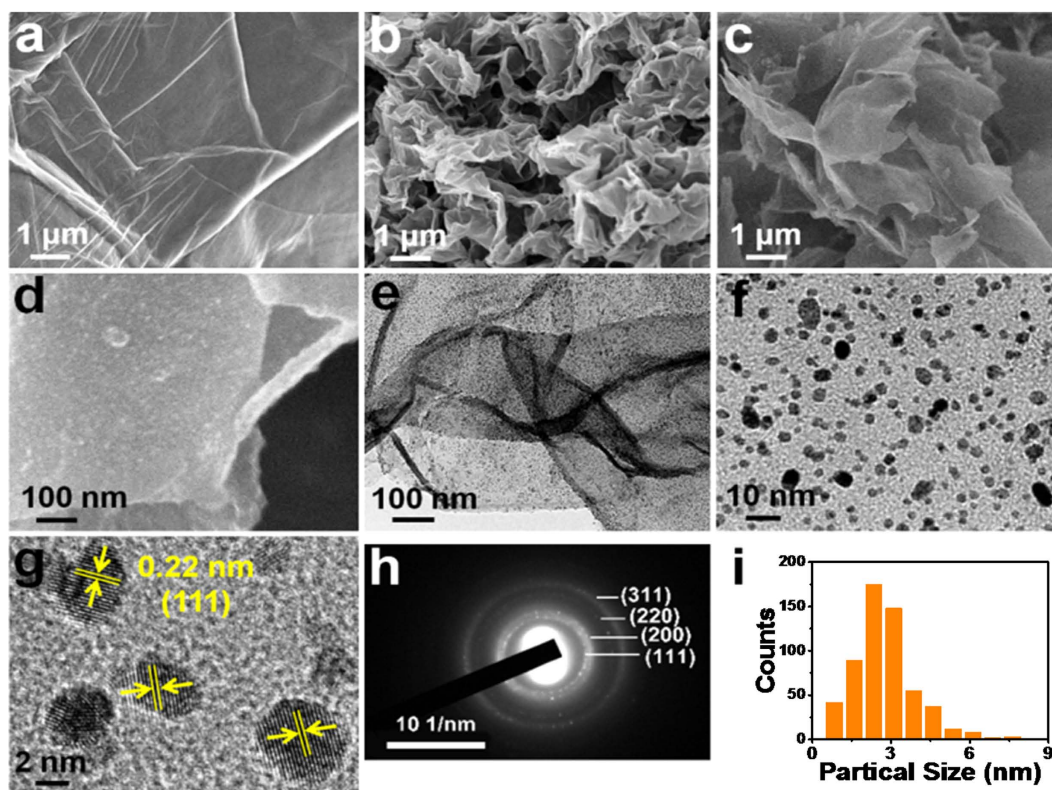

Figure 2. Morphology and structure of GO, N-rGO and Pt/N-rGO. SEM images of GO (**a**), N-rGO (**b**) and Pt/N-rGO (**c,d**). TEM (**e,f**), HRTEM (**g**) and SAED images (**h**) of Pt/N-rGO. And the histograms of Pt nanoparticle size distribution in (**f**) for Pt/N-rGO (**i**).

Results

The illustration for the synthesis of Pt/N-rGO is shown in Fig. 1. Graphene oxide (GO) was prepared by the modified Hummers method[21]. Pyrrole monomer was then adsorbed on the GO surface and polymerized by dropwise addition of $FeCl_3$ solution. After completely polymerized, the sample was subjected to pyrolysis under N_2 atmosphere to obtain the nitrogen doped reduced graphene oxide (N-rGO)[22]. SEM images of GO and N-rGO are presented in Fig. 2a,b, where the flat and smooth GO changed to the curved but still smooth N-rGO. The Pt nanoparticles were anchored on the surface of the N-rGO under the solvothermal condition with K_2PtCl_4 as the Pt source and ethylene glycol as both the reductant and solvent. The Pt loading content was 5.31 wt.% based on the ICP-AES measurement. The morphology and microstructure analyses of Pt/N-rGO were carried out with the
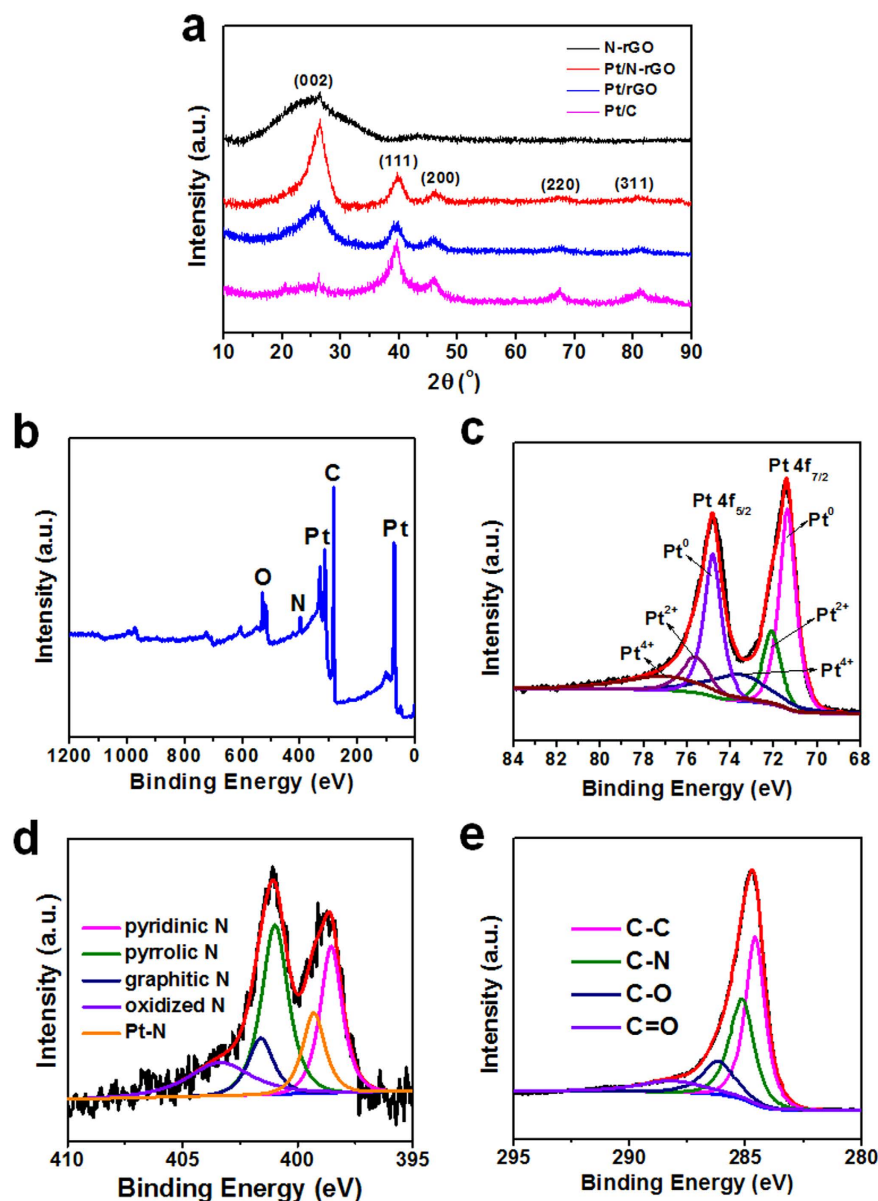
Figure 3. XRD and XPS spectra of N-rGO, Pt/rGO, Pt/N-rGO and the commercial Pt/C. (**a**) XRD patterns of N-rGO, Pt/rGO, Pt/N-rGO and the commercial Pt/C. XPS survey scan spectrum (**b**) as well as the high resolution Pt 4 f (**c**), N 1s (**d**) and C 1s core-level (**e**) spectra of Pt/N-rGO.

SEM and TEM images shown in Fig. 2c–f. The surface of Pt/N-rGO is very flat based on the SEM image observation in Fig. 2c. No large particles could be found from the enlarged SEM (Fig. 2d) and TEM (Fig. 2e) images of Pt/N-rGO. The Pt nanoparticles with the average diameter of about 2.8 nm distributed on the surface of N-rGO nanosheet uniformly were observed on the further enlarged TEM image (Fig. 2f). The related histograms of Pt nanoparticle size distribution may be found for Pt/N-rGO (Fig. 2i). The exposed interplanar distance of 0.22 nm was observed in the HRTEM image of Pt/N-rGO (Fig. 2g) corresponding to the lattice spacing of (111) facets of face-centered cubic (*fcc*) crystalline Pt, which is favor of the ORR electrocatalytic activity[19,20,23]. The SAED in Fig. 2h presents the polycrystalline structure of Pt/N-rGO with (111), (200), (220) and (311) facets of *fcc*-Pt (JCPDS No. 04-0802). The morphologies and microstructures of the Pt/N-rGO-L and Pt/N-rGO-M samples were also analysized by SEM and TEM techniques for comparison (Supplementary Fig. S1). The Pt particles with average diameter of 2.5 nm (Supplementary Fig. S1a–d) could be observed for Pt/N-rGO-L and some blank places were found on the surface of the matrix due to the less reaction time. The interplanar distances of 0.22 nm were also observed for the Pt nanoparticles in Pt/N-rGO-L and Pt/N-rGO-M (Supplementary Fig. S1c,g), even though the Pt particels of Pt/N-rGO-M became not very uniform with the average diameter increased to 3.5 nm (Supplementary Fig. S1e–h) after the more reaction time.

XRD patterns are shown in Fig. 3a, where the (111), (200), (220) and (311) facets of *fcc*-Pt could be clearly seen on both Pt/N-rGO and Pt/rGO samples, corresponding to that of the commercial Pt/C. Besides, the (002) facet

Factor of the ORR catalytic activity	Sample		
	Pt/N-rGO	Pt/rGO	Pt/C
E_{onset} (mV vs Ag/AgCl)	635.1	588.4	592.9
ΔE_{onset} (mV)	1.7	39.4	51.1
% loss of E_{onset} after ADT	0.3	6.7	8.6
$E_{half-wave}$ (mV vs Ag/AgCl)	470.1	440.1	430.3
$\Delta E_{half-wave}$ (mV)	5.0	30.0	70.2
% loss of $E_{half-wave}$ after ADT	1.1	6.8	16.3
Mass activity at 0.5 V vs Ag/AgCl (mA mg_{Pt}^{-1})	163.4	108.1	106.0
% loss of mass activity at 0.5 V after ADT	0.4	52.9	65.0
Specific activity at 0.5 V vs Ag/AgCl (mA cm^{-2})	3.73	2.10	2.20
% loss of specific activity at 0.5 V after ADT	−4.3	48.6	48.6

Table 1. The ORR catalytic activities over the Pt/N-rGO, Pt/rGO and Pt/C samples before and after ADT of 5000 cycles measured by RDE operated in the O_2 saturated 0.1 M $HClO_4$.

of graphitic carbon may be obtained for all of the Pt/N-rGO, Pt/rGO and N-rGO samples. XPS survey scan spectrum (Fig. 3b) shows that there are only signals of Pt, O, N and C elements. The Pt 4f XPS peaks (Fig. 3c) are fitted with three transitions corresponding to the different oxidation states of Pt (Pt^0, Pt^{2+} as PtO or $Pt(OH)_2$ and Pt^{4+} as PtO_2). Pt^0, as the main oxidation state in the composite (54.5%), presented a much more content than that of Pt^{2+} (20.9%) and Pt^{4+} (24.6%). The N 1s spectrum (Fig. 3d) suggests the presence of five types of N, $i.e.$, pyridinic N (398.5 eV), pyrrolic N (400.9 eV), graphitic N (401.6 eV), oxidized N (403.4 eV) and Pt-N bond (399.3 eV)[24]. Among them, the main type of plannar pyridinic N (24.7%) and pyrrolic N (34.7%) may possess a low electrical resistance and high electrocatalytic activity of the N-rGO since the nitrogens with planar sp^2 hybridization would not interrupt the p-p conjugation and avoidan intrinsic barrier impairing a continuous pathway for electron transport. Furthermore, the carbon atoms next to pyridinic and pyrrolic N may be activated where O_2 molecules could be adsorbed and reduced during the ORR[9–14]. It should be emphasized that the doped N heteroatoms can work as a bridge between the Pt nanoparticles and N-rGO, resulting in the low electrochemical impedance and the excellent stability of the Pt/N-rGO hybrid, which will be discussed later. The formation of C-C, C-N, C-O and C=O bands for Pt/N-rGO are also indicated by the C 1s XPS core-level spectra (Fig. 3e).

The activities of the catalysts were measured by RDE operated in O_2 saturated 0.1 M $HClO_4$ with the area of the glassy carbon electrode (GCE) of 0.196 cm^2 shown in Table 1. Figure 4a shows the polarization curves of Pt/N-rGO, Pt/rGO and the commercial Pt/C with the rotating speed of 1600 rpm. It can be seen that Pt/N-rGO exhibits a much better onset potential of 635.1 mV vs Ag/AgCl than that of Pt/rGO (588.4 mV) and the commercial Pt/C (592.9 mV). The electrocatalytic activity is also approximately estimated by the half-wave potential with the value of 470.1, 440.1 and 430.3 mV vs Ag/AgCl for Pt/N-rGO, Pt/rGO and the commercial Pt/C, respectively, suggesting the best catalytic activitiy of Pt/N-rGO among them. Besides, Pt/N-rGO-L and Pt/N-rGO-M also exhibited better catalytic activities than that of the commercial Pt/C (Supplementary Fig. S2 and Table S1). The onset potentials of Pt/N-rGO-L and Pt/N-rGO-M were 623.7 and 618.4 mV vs Ag/AgCl, which are a little lower than that of Pt/N-rGO. Additionally, the composites of Pt/N-rGO and Pt/rGO also exihibted much better ORR catalytic activity than rGO and N-rGO, indicating the Pt nanoparticlas made most of the contribution to the ORR performance (Supplementary Fig. S3). The kinetic current can be calculated from the ORR polarization curves according to the Koutecky-Levich equation[25,26]: $1/i = 1/i_d + 1/i_k$, where i_d is the diffusion-limiting current and i_k is the kinetic current. The Tafel slope for Pt/N-rGO in Fig. 4b obtained in 0.1 M $HClO_4$ was slightly higher than those of Pt/rGO and the commercial Pt/C, with the higher activity at both high and low current density regions depending on the degree of surface coverage of the adsorbed ions. The polarization curves of Pt/N-rGO are shown in Fig. 4c with the Koutecky-Levich plots in Fig. 4d. The value of the number of exchanged electrons was about 4, indicating that Pt/N-rGO follows the four-electron route. The results were also demonstrated by RRDE in Fig. 4e. The amount of H_2O_2 produced on the disk electrode was simultaneously detected on the ring electrode. The mole fraction of H_2O_2 can be calculated as follows[5,27]: $X_{H_2O_2}$ (%) $= 2i_R/N/(i_D + i_R/N) \times 100$, where N is the collection efficiency ($N = 0.2$), and i_R and i_D are the ring and disk current, respectively. The lower content H_2O_2 formation over Pt/N-rGO than that of Pt/rGO and the commerical Pt/C corresponded to the number of exchanged electons of about 4. Figure 4f showed the impedance of Pt/N-rGO (0.5 Ω), which was much lower than that of Pt/rGO (5.2 Ω) and the commercial Pt/C (8.5 Ω). The significantly low resistance of Pt/N-rGO demonstrated the tight connection by Pt-N bonds between Pt nanoparticles and N-rGO with a pathway for the electronic transports, which are crucial for the electrochemical activity.

The low content of Pt nanoparticles (5.31 wt.%) anchored on the surface of N-rGO uniformly in Pt/N-rGO resulted in the much better catalytic activity than that of the commercial Pt/C where the content of Pt is 20 wt.%. The high catalytic activity of Pt/N-rGO can be attributed to the apparently synergistic catalytic effect of N-doped carbon matrix[28,29] and the high activated Pt with the very suitable size of about 2.8 nm[15–18,30–32] which is in favour of the Pt dispersion thus increasing the number of active sites, and overwhelmingly exposed (111) facets with high intrinsic catalytic activity[19,20,23]. The interaction between C-N and Pt nanoparticles can lead to lower resistance and higher binding energy, decreasing the detrimental strongly adsorbed intermediates, thus leading to the enhancement of the catalytic property[33,34].
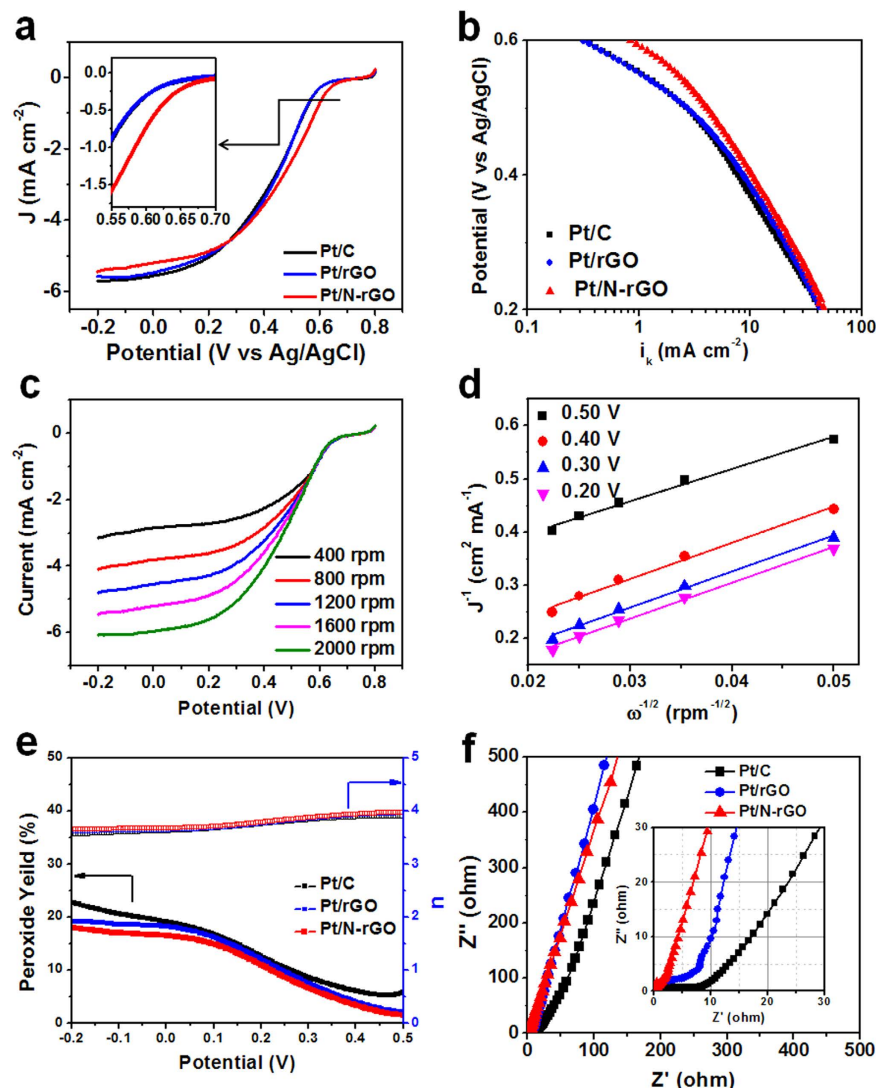
Figure 4. ORR polarization curves of Pt/N-rGO, Pt/rGO and Pt/C. (**a**) The polarization curves of the commercial Pt/C, Pt/rGO and Pt/N-rGO at the rotating speed of 1600 rpm with the insert of the enlarged polarization curves at around the onset potentials for clarity. (**b**) The Tafel plots for Pt/C, Pt/rGO and Pt/N-rGO at the rotating speed of 1600 rpm. (**c**) The rotation rate-dependent ORR polarization curves for Pt/N-rGO. (**d**) The Koutecky–Levich plots from the ORR data at different potentials. (**e**) The peroxide yield with regard to the total oxygen reduction products and the calculated electron transfer number of Pt/C, Pt/rGO and Pt/N-rGO from RRDE in O_2-saturated 0.1 M $HClO_4$. And (**f**) EIS of electrodes of Pt/C, Pt/rGO and Pt/N-rGO.

The stabilities of Pt/N-rGO, Pt/rGO and the commercial Pt/C were investigated by the accelerated durability tests (ADT) at the scan rate of 100 mV s^{-1} for 5000 cycles from 0.2 to 0.6 V vs Ag/AgCl. CV curves were measured in N_2 saturated 0.1 M $HClO_4$ solution at a scan rate of 50 mV s^{-1} before and after ADT of 5000 cycles in Fig. 5a. The electrochemical surface area (ECSA) was calculated by measuring the Coulombic charge for hydrogen desorption in the range of −0.2 to 0.15 V vs Ag/AgCl[35]. The nomalized ECSA evaluated after every 500 cycles are shown in Fig. 5b. The specific values of the ECSA of Pt/N-rGO, Pt/rGO and commercial Pt/C based on the mass of Pt were 65.7, 55.3 and 66.2 m^2 g^{-1}, which are comparable to the typical reported composites of Pt and graphene (Supplementary Table S3). The ECSA of Pt/N-rGO decreased by 4.6%, lower than that of Pt/rGO (8.3%) and much lower than that of the commercial Pt/C (31.9%). The slight drop of ECSA over Pt/N-rGO may be due to the decrease of small amount of Pt^0, forming some oxide of Pt on the surface recealed by XPS after ADT (Supplementary Fig. S4 and Table S2). Comparing to Fig. 3c, the content of Pt^0 decreased slightly to 50.9% and Pt^{2+} and Pt^{4+} increased to 22.8% and 26.3%, respectively, thus the oxidation of Pt resulting in the slight decrease of ECSA[36]. The polarization curves of Pt/N-rGO, Pt/rGO and Pt/C before and after ADT of 5000 cycles are also shown in Fig. 5c. The loss of onset potential of Pt/N-rGO is only 1.7 mV, which is much better than that of Pt/rGO (39.4 mV) and the commercial Pt/C (51.1 mV). A slight negative shift of 5.0 mV (only 1.1% loss) was observed on the half-wave potential of Pt/N-rGO, which is better than that of 30.0 mV (6.8% loss) of Pt/rGO and 70.2 mV (16.3% loss) of the commercial Pt/C. The mass and specific activities in Fig. 5d can be obtained by normalizing
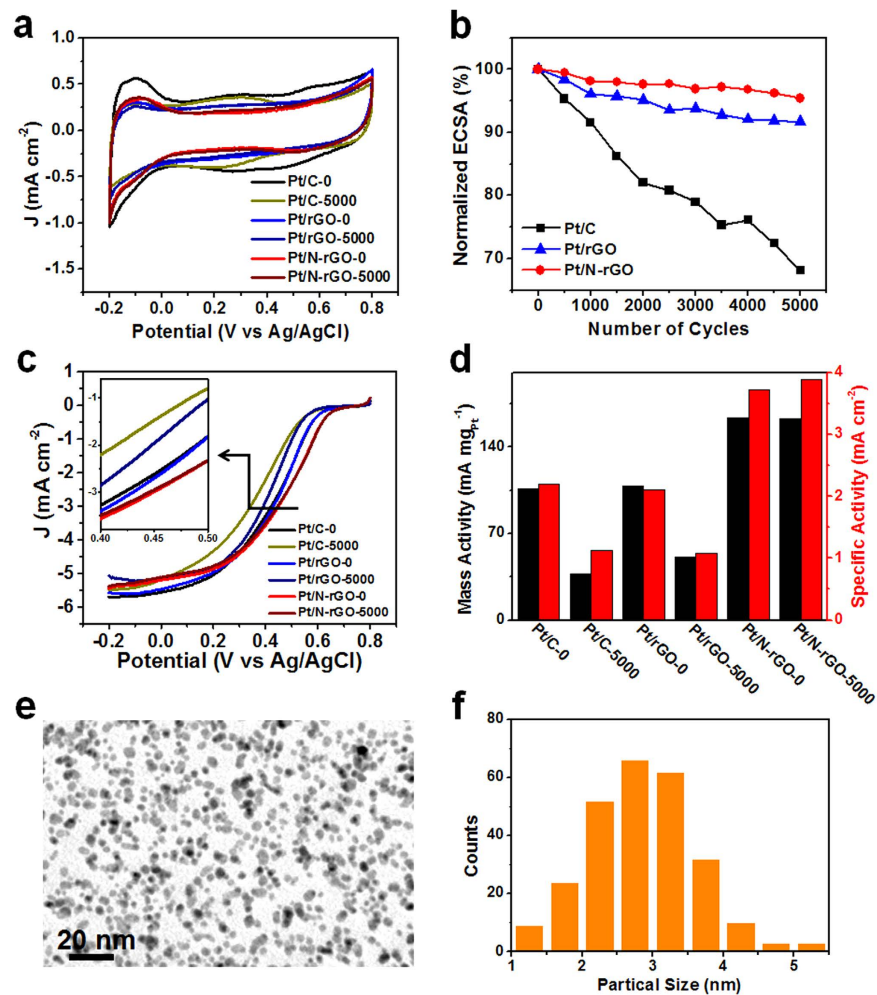
Figure 5. Durability test for Pt/N-rGO, Pt/rGO and Pt/C. (a) CV curves of Pt/N-rGO, Pt/rGO and Pt/C before and after ADT of 5000 cycles in N_2-saturated 0.1 M $HClO_4$. (**b**) Comparative ECSA of Pt/N-rGO, Pt/rGO and Pt/C during 5000 electrochemical cycles. (**c**) The polarization curves of the commercial Pt/C, Pt/rGO and Pt/N-rGO before and after the ADT of 5000 cycles in O_2-saturated 0.1 M $HClO_4$ with the insert of the enlarged polarization curves at around the half-wave potentials for clarity. (**d**) The mass activities and specific activities of the commercial Pt/C, Pt/rGO and Pt/N-rGO at 0.5 V vs Ag/AgCl. And TEM image (**e**) and the histograms (**f**) of Pt nanoparticle size distribution for Pt/N-rGO after ADT of 5000 cycles.

the kinetic current to the mass of Pt and ECSA, respectively. The mass activity of Pt/N-rGO at 0.5 V vs Ag/AgCl reached 163.4 mA mg_{Pt}^{-1}, which is much higher than that of Pt/rGO (108.1 mA mg_{Pt}^{-1}) and the commercial Pt/C (106.0 mA mg_{Pt}^{-1}). It should be mentioned that the loss of mass activity at 0.5 V vs Ag/AgCl of Pt/N-rGO is only 0.4% after ADT of 5000 cycles, which is much lower than that of Pt/rGO (52.9%) and the commercial Pt/C (65.0%). The specific activity of Pt/N-rGO at 0.5 V vs Ag/AgCl was 3.73 mA cm^{-2}, which was retained well to 3.89 mA cm^{-2}. For comprison, the specific activity of Pt/rGO (2.10 mA cm^{-2}) and Pt/C (2.20 mA cm^{-2}) degreased to 1.08 and 1.13 mA cm^{-2}, respectively.

TEM images of Pt/N-rGO and Pt/rGO were obtained before and after the ADT. There was no obvious change of Pt/N-rGO after ADT in Fig. 5e. The size distribution of Pt nanoparticles after ADT in Fig. 5f with the mean diameter of 2.9 nm is similar to that before ADT. However, the mean diameter of the Pt nanoparticles on Pt/rGO increased from 3.7 to 5.2 nm after ADT with certain detachment, dissolution, migration and aggregation of Pt nanoparticles (Supplementary Fig. S5). Also, the Pt nanoparticles on the commercial Pt/C aggregated and agglomerated severely into irregular larger nanoparticles after ADT[37].

The much better stability of Pt/N-rGO than that of the commercial Pt/C and Pt/rGO can be attributed to the doped N working as a bridge between N-rGO matrix and Pt nanoparticles with the Pt-N and C-N chemical bonds. The reported related density function theory calculation also indicates that the binding energy of Pt and the N-doped carbon is much higher than that of the non-doped matrix[38–41]. Thus, the composite structure of Pt nanoparticles anchored on the N-doped carbon matrix may not only prevent the nanoparticles from detachment, dissolution, migration and aggregation, but also provide a good pathway for the electronic transports, contributing to the improvement in both catalytic activity and stability of the catalyst[37,42]. Nitrogen atom with more electrons than carbon atom was doped in the bone of graphite carbon, altering the electron donating character.

The plannar N on the edge also provided an extra long pair of electrons enhancing the delocalized π bond and the interaction between Pt nanoparticles and the carbon matrix[36,43].

The ORR performances of Pt/N-rGO were compared with the typical reported composites of Pt and N-doped carbons (Supplementary Table S4). Pt/N-rGO showed the the higher specific activity than most of them due to the synergistic catalytic effect of N-doped carbon matrix and Pt nanoparticles with high activity. The stability of Pt/N-rGO was also better than most of them. The noble metal Pt in Pt/N-rGO takes only 5.31 wt.% of the total weight in Pt/N-rGO, which is one of the lowest among the composites of Pt and N-doped carbon in Tables S3 and S4. In addition, the content of Pt in Pt/N-rGO is also much lower than that of the other usual Pt containing catalysts, *e.g.*, 33 wt.% of Pt/RGO[3], 24 wt.% of Pt-Rh-Ni/C[19], 14.3 wt.% of Pt/PANIlong[24], 37 wt.% of FePtAu[35], 44.37 wt.% of Pt/CNC(1000)[36] and 13.01 wt.% of Pt@CN$_x$/CNT[37], and close to that of low content of 5.06 wt.% of TiNiN@Pt[25]. The low loading of Pt in the Pt/N-rGO catalyst may bring about low cost of the catalyst, which is benefit for its commercial utilization.

Discussions

We have successfully synthesized an unusual ORR hybrid catalyst Pt/N-rGO, in which Pt nanoparticles with uniform size deposited on the surface of nitrogen doped reduced graphene oxide evenly with N working as the bridge between them. The catalyst with low content of Pt demonstrated a much better catalytic performance than the commercial Pt/C due to the synergistic catalytic effect of heteroatom doped carbon matrix and Pt particles with the high activity diameter of uniformed 2.8 nm and exposed (111) crystal planes. The N atoms offered a pathway for the transportation of electrons resulting in the low electrical resistance and prevented the detachment, dissolution, migration and aggregation of Pt nanoparticles on the matrix during the long-term cycling, leading to an excellent stability of the catalyst. Besides, the low loading of Pt in the Pt/N-rGO catalyst may be helpful for getting rid of the constraint of the limited Pt resource in nature, thus promoting its commercial utilization. Such Pt/N-rGO hybrid material possessing of comprehensive ideal Pt particle size and the crystal faces as well as suitable matrix provides a good concept to construct the ORR catalyst with high electroactivity and excellent stability, contributing greatly for the fuel cells and/or metal-air batteries.

Methods

Materials preparation.   *GO synthesis.*   Graphene oxide was prepared as follows. Firstly, 1.0 g of graphite powder was added to 150 mL flask. Then, 24 mL of concentrated sulfuric acid was added and the mixture was stirred at room temperature for 6 h. And then, 0.5 g NaNO$_3$ was added to the mixture and stirred for 3 h. After that, 3.0 g of KMnO$_4$ was added and the reaction was heated to 45 °C for 30 min. The reaction mixture was further heated to 90 °C in oil bath and held for 30 min after 50 mL of deionized water was added. The obtained mixture was cooled down to room temperature after 100 mL deionized water was dropped in. Finally, 5 mL of H$_2$O$_2$ (30%) was added in order to complete the oxidation reaction, and the resulting mixture was centrifuged and washed thoroughly with HCl (10%) and water. The obtained precipitate was dispersed in 200 mL of water, which was sonicated for 1 h and freeze dried for 12 h.

N-rGO synthesis.   30 mg of the prepared GO was dispersed in 35 mL of deionized water and 0.6 mL of pyrrole was dropped into the mixture followed by 5 min of sonication and 10 min vigorous stirring. Then, 25 mL of 0.24 M FeCl$_3$ solution was added to the mixture and the stirring was last for 4 h at room temperature to complete the polymerization. The production was separated by filtration and washed with ethanol and water. After dried, the production was subjected to pyrolysis under flowing N$_2$ atmosphere at 800 °C for 1 h. Then, the product was immersed in 0.5 M H$_2$SO$_4$ solution at 80 °C for 8 h to remove the unstable and ORR-nonreactive phases. After washed with deionized water and dried, the sample was pyrolyzed for a second time under flowing N$_2$ atmosphere at 800 °C for 3 h.

Pt/N-rGO synthesis.   Pt nanoparticles were synthesized on N-rGO using a facile solvothermal method. 45 mg of N-rGO was dispersed in 50 mL of ethylene glycol and 10 mL of deionized water. Subsequently, 10 mL of potassium tetrachloroplatinate (II) (K$_2$PtCl$_4$) aqueous solution (concentration of 1 mg mL^{-1} and aged for at least 24 h) was dropped into the mixture and sonicated for 1 h. Then the mixture was heated to 140 °C with stirring and maintained for 4 h. At last, the product was centrifuged and washed with deionized water and ethanol and dried in a vacuum oven. The product with the reaction time of 4 h was named Pt/N-rGO. The related sample with the reaction time of 2 and 6 h was also obtained and named as Pt/N-rGO-L and Pt/N-rGO-M, respectively, for comparison. The Pt/rGO sample was prepared under the similar experimental conditions as those of Pt/N-rGO with the reaction time of 4 h, where rGO was used as the matrix instead of N-rGO.

Materials characterization.   Scanning electron microscopy (SEM) images were taken on the HITACHI S-4800F with the operating voltage of 5 kV. Transmission electron microscopy (TEM) and high resolution TEM images were obtained on the JEOL JEM-2100F. X-ray diffraction (XRD) patterns were identified on the Panalytical X'Pert Pro X-ray Powder Diffractometer with Cu-Kα radiation. X-ray photoelectron spectroscopy (XPS) curves were examined by the ESCALAB 250Xi of Thermofisher. And inductively coupled plasma atomic emission spectroscopy (ICP-AES) was gotten on the Thermo Scientific.

Electrochemical measurements.   All electrochemical measurements were performed in a three-electrode system on an electrochemical workstation (Pine Instrumentation, Wavedriver 20). The catalysts dispersed on the glassy carbon (GC) rotating disk electrode and rotating ring and disk electrode (RDE and RRDE, Pine Instrumentation) was performed as the work electrode with the geometric area of 0.196 cm and 0.247 cm, respectively. Ag/AgCl (saturated KCl) and Pt wire was used as the reference and counter electrode, respectively. To

prepare the work electrode, the catalyst was suspended in the mixture of deionized water, ethanol and 5% of Nafion aqueous solution (v/v/v = 8/1/1) by sonication. The suspension was dropped onto the GC electrode which had been polished with Al_2O_3 powder and dried at room temperature. All electrodes were with the mass of loaded Pt of ~25 μg cm^{-2} measured by ICP-AES.

Cyclic voltammetry (CV) curves were conducted with the scan rate of 50 mV s^{-1} from −0.2 to 0.8 V in N_2-saturated 0.1 M HClO$_4$. Linear sweep voltammetry (LSV) measurements with the scan rate of 10 mV s^{-1} were performed with the RDE and RRDE rotation rates varying from 400 to 2000 rpm in O_2-saturated 0.1 M HClO$_4$. The accelerated durability tests were measured at the scan rate of 100 mV s^{-1} for 5000 cycles from 0.2 to 0.6 V vs Ag/AgCl in 0.1 M HClO$_4$. The electrochemical surface area of Pt in the catalysts was calculated by the equation: ECSA $= Q_H/(C \times m)$, where Q_H (μC) is the charge for the hydrogen desorption of the CVs, C is the electrical charge (equals to 210 μC cm^{-2}) for the monolayer adsorption of hydrogen on Pt nanocrystal surface, and m is the mass of Pt loaded on the working electrode. For ORR the mass and specific activity was obtained by normalizing i_k (obtained from the Koutecky-Levich equation ($1/i = 1/i_d + 1/i_k$) to Pt and ECSA, respectively. To analyze the number of transferred electrons, the Koutecky-Levich equations were shown as below:

$$1/J = 1/J_L + 1/J_K = 1/(B\omega^{1/2}) + 1/J_K \tag{1}$$

$$B = 0.2nFC_0(D_0)^{3/2}\upsilon^{-1/6} \tag{2}$$

$$J_K = nFkC_0 \tag{3}$$

where J (mA cm^{-2}) is the measured current density, J_K and J_L (mA cm^{-2}) is the kinetic- and diffusion limiting current density, respectively, ω is the angular velocity of the rotating disk ($\omega = 2\pi N$, N is the linear rotating speed in rpm), n is the overall number of the electrons transferred in oxygen reduction reaction, F is the Faraday constant ($F = 96485$ C mol^{-1}), C_0 is the bulk concentration of O_2 (1.26×10^{-3} mol L^{-1} in 0.1 M HClO$_4$), D_0 is diffusion coefficient of O_2 (1.7×10^{-5} cm^2 s^{-1} in 0.1 M HClO$_4$), υ is the kinematic viscosity of the electrolyte (1.009×10^{-2} cm^2 s^{-1} in 0.1 M HClO$_4$), and k is the electron transfer rate constant. According to equations (1) and (2), the number of transferred electrons (n) and J_K can be obtained from the slope and intercept of the Koutecky-Levich plots, respectively.

References

1. Gasteiger, H. A. & Marković, N. M. Just a dream or future reality? *Science* **324,** 48–49 (2009).
2. McCloskey, B. D. *et al.* On the efficacy of electrocatalysis in nonaqueous Li–O$_2$ batteries. *J. Am. Chem. Soc.* **133,** 18038–18041 (2011).
3. Li, Y. *et al.* Stabilization of high-performance oxygen reduction reaction Pt electrocatalyst supported on reduced graphene oxide/carbon black composite. *J. Am. Chem. Soc.* **134,** 12326–12329 (2012).
4. Guo, S., Dong, S. & Wang, E. Three-dimensional Pt-on-Pd bimetallic nanodendrites supported on graphene nanosheet: facile synthesis and used as an advanced nanoelectrocatalyst for methanol oxidation. *ACS Nano* **4,** 547–555 (2010).
5. Yang, J. *et al.* A highly efficient metal-free oxygen reduction electrocatalyst assembled from carbon nanotubes and graphene. *Adv. Mater.* **28,** 4606–4613 (2016).
6. Zhou, Y. *et al.* Enhancement of Pt and Pt-alloy fuel cell catalyst activity and durability *via* nitrogen-modified carbon supports. *Energy Environ. Sci.* **3,** 1437–1446 (2010).
7. Zhao, Z., Li, M., Zhang, L., Dai, L. & Xia, Z. Design principles for heteroatom-doped carbon nanomaterials as highly efficient catalysts for fuel cells and metal–air batteries. *Adv. Mater.* **27,** 6834–6840 (2015).
8. Daems, N., Sheng, X., Vankelecom, I. F. J. & Pescarmona, P. P. Metal-free doped carbon materials as electrocatalysts for the oxygen reduction reaction. *J. Mater. Chem. A* **2,** 4085–4110 (2014).
9. Yu, D., Zhang, Q. & Dai, L. Highly efficient metal-free growth of nitrogen-doped single-walled carbon nanotubes on plasma-etched substrates for oxygen reduction. *J. Am. Chem. Soc.* **132,** 15127–15129 (2010).
10. Qu, L., Liu, Y., Baek, J. B. & Dai, L. Nitrogen-doped graphene as efficient metal-free electrocatalyst for oxygen reduction in fuel cells. *ACS Nano* **4,** 1321–1326 (2010).
11. Chen, S. *et al.* Nitrogen-doped carbon nanocages as efficient metal-free electrocatalysts for oxygen reduction reaction. *Adv. Mater.* **24,** 5593–5597 (2012).
12. Nie, Y., Li, L. & Wei, Z. Recent advancements in Pt and Pt-free catalysts for oxygen reduction reaction. *Chem. Soc. Rev.* **44,** 2168–2201 (2015).
13. Guo, D. *et al.* Active sites of nitrogen-doped carbon materials for oxygen reduction reaction clarified using model catalysts. *Science* **351,** 361–365 (2016).
14. Ding, W. *et al.* Space-confinement-induced synthesis of pyridinic- and pyrrolic-nitrogen-doped graphene for the catalysis of oxygen reduction. *Angew. Chem. Int. Ed.* **125,** 11971–11975 (2013).
15. Peuckert, M., Yoneda, T., Betta, R. A. D. & Boudart, M. Oxygen reduction on small supported platinum particles. *J. Electrochem. Soc.* **133,** 944–947 (1986).
16. Kinoshita, K. Particle size effects for oxygen reduction on highly dispersed platinum in acid electrolytes. *J. Electrochem. Soc.* **137,** 845–848 (1990).
17. Gasteiger, H. A., Kocha, S. S., Sompalli, B. & Wagner, F. T. Activity benchmarks and requirements for Pt, Pt-alloy, and non-Pt oxygen reduction catalysts for PEMFCs. *Appl. Catal. B-Environ.* **56,** 9–35 (2005).
18. Perez-Alonso, F. J. *et al.* The effect of size on the oxygen electroreduction activity of mass-selected platinum nanoparticles. *Angew. Chem. Int. Ed.* **51,** 4641–4643 (2012).
19. Beermann, V. *et al.* Rh-doped Pt–Ni octahedral nanoparticles: understanding the correlation between elemental distribution, oxygen reduction reaction, and shape stability. *Nano Lett.* **16,** 1719–1725 (2016).
20. Stamenkovic, V. R. *et al.* Improved oxygen reduction activity on Pt$_3$Ni (111) via increased surface site availability. *Science* **315,** 493–497 (2007).
21. Marcano, D. C. *et al.* Improved synthesis of graphene oxide. *ACS Nano* **4,** 4806–4814 (2010).
22. Wu, Z.-Y. *et al.* Iron carbide nanoparticles encapsulated in mesoporous Fe-N-doped carbon nanofibers for efficient electrocatalysis. *Angew. Chem. Int. Ed.* **127,** 8297–8301 (2015).
23. He, D. S. *et al.* Ultrathin icosahedral Pt-enriched nanocage with excellent oxygen reduction reaction activity. *J. Am. Chem. Soc.* **138,** 1494–1497 (2016).

24. Melke, J. *et al.* Metal–support interactions of platinum nanoparticles decorated N-doped carbon nanofibers for the oxygen reduction reaction. *ACS Appl. Mater. Interfaces* **8,** 82–90 (2016).

25. Tian, X. *et al.* Transition metal nitride coated with atomic layers of Pt as a low-cost, highly stable electrocatalyst for the oxygen reduction reaction. *J. Am. Chem. Soc.* **138,** 1575–1583 (2016).

26. Guo, S. & Sun, S. FePt nanoparticles assembled on graphene as enhanced catalyst for oxygen reduction reaction. *J. Am. Chem. Soc.* **134,** 2492–2495 (2012).

27. Beyhan, S., Sahin, N. E., Pronier, S., Leger, J.-M. & Kadirgan, F. Comparison of oxygen reduction reaction on Pt/C, Pt-Sn/C, Pt-Ni/C, and Pt-Sn-Ni/C catalysts prepared by Bönnemann method: A rotating ring disk electrode study. *Electrochim. Acta* **151,** 565–573 (2015).

28. Jiang, Z. & Jiang, Z. Interaction induced high catalytic activities of CoO nanoparticles grown on nitrogen-doped hollow graphene microspheres for oxygen reduction and evolution reactions. *Sci. Rep.* **6,** 27081 (2016).

29. Choi, C. H., Park, S. H. & Woo, S. I. Phosphorus–nitrogen dual doped carbon as an effective catalyst for oxygen reduction reaction in acidic media: effects of the amount of P-doping on the physical and electrochemical properties of carbon. *J. Mater. Chem.* **22,** 12107–12115 (2012).

30. Li, X., Park, S. & Popov, B. N. Highly stable Pt and PtPd hybrid catalysts supported on a nitrogen-modified carbon composite for fuel cell application. *J. Power Sources* **195,** 445–452 (2010).

31. Stephens, I. E. L., Bondarenko, A. S., Grønbjerg, U., Rossmeisl, J. & Chorkendorff, I. Understanding the electrocatalysis of oxygen reduction on platinum and its alloys. *Energy Environ. Sci.* **5,** 6744–6762 (2012).

32. Vinayan, B. P. & Ramaprabhu, S. Platinum-TM (TM = Fe, Co) alloy nanoparticles dispersed nitrogen doped (reduced graphene oxide-multiwalled carbon nanotube) hybrid structure cathode electrocatalysts for high performance PEMFC applications. *Nanoscale* **5,** 5109–5118 (2013).

33. Zhou, Y. K. *et al.* Improving PEM fuel cell catalyst activity and durability using nitrogen-doped carbon supports: observations from model Pt/HOPG systems. *J. Mater. Chem.* **19,** 7830–7838 (2009).

34. Stamenovic, V. *et al.* Changing the activity of electrocatalysts for oxygen reduction by tuning the surface electronic structure. *Angew. Chem. Int. Ed.* **45,** 2897–2901 (2006).

35. Guo, S., Zhang, S., Su, D. & Sun, S. Seed-mediated synthesis of core/shell FePtM/FePt (M = Pd, Au) nanowires and their electrocatalysis for oxygen reduction reaction. *J. Am. Chem. Soc.* **135,** 13879–13884 (2013).

36. Wang, X.-X., Tan, Z.-H., Zeng, M. & Wang, J.-N. Carbon nanocages: A new support material for Pt catalyst with remarkably high durability. *Sci Rep.* **4,** 4437 (2014).

37. Guo, L. *et al.* Embedding Pt nanocrystals in N-doped porous carbon/carbon nanotubes toward highly stable electrocatalysts for the oxygen reduction reaction. *ACS Catal.* **5,** 2903–2909 (2015).

38. Gracia-Espino, E., Jia, X. & Wågberg, T. Improved oxygen reduction performance of Pt–Ni nanoparticles by adhesion on nitrogen-doped graphene. *J. Phys. Chem. C* **118,** 2804–2811 (2014).

39. Acharya, C. K., Sullivan, D. I. & Turner, C. H. Characterizing the interaction of Pt and PtRu clusters with boron-doped, nitrogen-doped, and activated carbon: density functional theory calculations and parameterization. *J. Phys. Chem. C* **112,** 13607–13622 (2008).

40. Li, Y. H., Hung, T. H. & Chen, C. W. A first-principles study of nitrogen- and boron-assisted platinum adsorption on carbon nanotubes. *Carbon* **47,** 850–855 (2009).

41. Tian, Y., Liu, Y., Zhao, J. & Ding, Y. High stability and superior catalytic reactivity of nitrogen-doped graphene supporting Pt nanoparticles as a catalyst for the oxygen reduction reaction: a density functional theory study. *RSC Adv.* **5,** 34070–34077 (2015).

42. Jin, H. *et al.* Graphene quantum dots supported by graphene nanoribbons with ultrahigh electrocatalytic performance for oxygen reduction. *J. Am. Chem. Soc.* **137,** 7588–7591 (2015).

43. Coloma, F., Sepulveda-Escribano, A., Fierro, J. L. G. & Rodriguez-Reinoso, F. Preparation of platinum supported on pregraphitized carbon blacks. *Langmuir* **10,** 750–755 (1994).

Acknowledgements

Author Contributions

Q.-M.G. planned and supervised the project; Q.-M.G. and Z.-P.L. advised on the project; Z.-Y.L. and Q.-M.G. designed and performed experiments; Z.-Y.L., H.Z., W.-Q.T., Y.-L.T. and W.-W.Q. carried out the electrochemical property tests. Q.-M.G. and Z.-Y.L. analyzed data and wrote the manuscript; and all authors discussed the results and commented on the manuscript.

Additional Information

Supplementary information accompanies this paper at http://www.nature.com/srep

Competing financial interests: The authors declare no competing financial interests.

How to cite this article: Li, Z. *et al.* Low content Pt nanoparticles anchored on N-doped reduced graphene oxide with high and stable electrocatalytic activity for oxygen reduction reaction. *Sci. Rep.* **7,** 43352; doi: 10.1038/srep43352 (2017).

Publisher's note: Springer Nature remains neutral with regard to jurisdictional claims in published maps and institutional affiliations.